

Exploiting decoupled discretization in meshless lattice Boltzmann method for high-Reynolds number flows

Dawid Strzelczyk*, Maciej Matyka

Institute of Theoretical Physics, Faculty of Physics and Astronomy, University of Wrocław, pl. M. Borna 9, 50-204, Wrocław, Poland

* dawid.strzelczyk@uwr.edu.pl

Abstract One of the most severe limitations of the Lattice Boltzmann Method in the context of simulating inertial flows is the coupling of the discretization of space to the velocity discretization. It causes the need to increase the size of computational meshes whenever one wants to increase the Reynolds number in the system for a fixed velocity and viscosity. This work aims at adopting the recently proposed meshless LBM formulation to the problem of high Reynolds number flows by using its internal property of decoupled space and velocity discretizations. In meshless formulation, one can change the reference length of the problem by scaling the distances between points that discretize the domain while the streaming distance remains fixed. By doing that, we increase the Reynolds number at no cost: additional nodes need not be inserted in the discretization. We measure the accuracy and efficiency of this approach in the flow around a circular obstacle at $Re = 80$ – 160 , the lid-driven cavity flow at $Re = 100$ – 5000 , and the flow through a porous sample at $Re = 0.8$ – 1500 . Additionally, we apply the meshless streaming step to the recently proposed fixed relaxation time $\tau = 1$ LBM to extend its applicability to model inertial flows.

Keywords: Lattice Boltzmann Method, meshless methods, inertial flows, Reynolds number

1 Introduction

The transport of fluids through complex, porous structures is ubiquitous with many technological applications (CO₂ storage, oil and shale gas extraction, electric battery design). It is of great interest for the study of human health, e.g. blood and cerebrospinal fluid flow, gas transport in the lungs [1, 2].

Experimental investigation of fluid flow phenomena in porous media is costly and requires sophisticated setups. Measuring velocity fields in creeping flows using Particle Image Velocimetry (PIV) methods has become popular [3, 4]. However, beyond Darcy Law (inertial regime) [5], PIV tracers used to track the flow face several problems. They may, for instance, damage the porous sample, and some of the flow regions may get excluded from the measurement due to the lack of tracers therein. Also, the tracers' size must be chosen carefully to reconcile the accuracy of the scattered signal acquisition and the minimal interaction between the tracers, flow, and the pore space [6]. The remedy for this is to use numerical methods to solve fluid flow transport equations directly in pore space. Real samples, however, are relatively big compared to pore size, and using standard numerical methods based on computational grids may become impractical. This becomes most problematic at large Reynolds numbers, where fine flow structures appear.

Recently, the Lattice Boltzmann Method (LBM) became one of the most popular numerical tools used to solve the Navier-Stokes equations at the pore scale [7, 8]. It was applied to the simulation of fluid transport in various contexts of porous media [9], multiphase flows [10], semiclassical fluids flow [11], particulate suspensions [12] and especially inertial flows, and turbulent flows [13, 14]. Its popularity arises from the stable and local treatment of non-linear effects, a huge potential for parallelization of calculations, and simple implementation of basic no-slip boundary conditions on a regular grid [15, 16, 17]. The latter is especially attractive in complex porous media geometries, i.e. those arising from tomography scans in the form of binary images. Unfortunately, the memory overhead associated with storing the distribution function in LBM, and the need to regularly discretize the entire simulation space, limits the utility of this method for real-life, large samples with relatively small pore sizes.

One way to overcome the mentioned problem of excessive memory usage is to resort to LBM models with the fixed relaxation time $\tau = 1$ (LBM1) [18, 19] where the distribution function is not explicitly stored in the memory. As shown in our previous work, LBM1 simplifies the main algorithm and reduces the memory requirement up to 86% compared to the standard LBM solver [18]. Savings may also come from the use of

the meshless discretization of space in LBM (meshless LBM, MLBM) [20]. This offers a significant advantage regarding the flexibility of space discretization, with LBM grid points distributed, i.e., in the pore-space only. We recently investigated its convergence in several scenarios, including low-Reynolds number flow through porous samples consisting of a network of two-dimensional channels and a three-dimensional periodic array of spheres [21].

By default, in both mentioned approaches, increasing the Reynolds number means either a decrease in viscosity, an increase in the flow velocity, or an increase in the size of the system. The first approach is limited by the minimum theoretical viscosity due to stability issues. Moreover, it becomes inaccessible in the $\tau = 1$ formulation [18], where, by definition, we restrict the model to a fixed relaxation time, which involves fixing viscosity. Thus, considering the maximum velocity limit due to Mach number restrictions, increasing the Reynolds number by increasing the size of the system is the only way to obtain stable, high-Reynolds number fluid flow solutions in both MLBM and LBM1.

The aim of this work is to investigate the procedure of the domain reference length scaling in the meshless LBM (MLBM) to change the Reynolds number at zero computational and algorithmic cost. The indirect goal of the work is to implement the meshless streaming step in the LBM1 model to achieve higher Reynolds numbers without additional memory overhead. We apply this scaling method to classic fluid flow problems: Kármán vortex street, lid-driven cavity and in the inertial regime of a flow through a porous medium.

2 Methods

2.1 Lattice Boltzmann Method

Lattice Boltzmann Method [15, 16] is a numerical tool for solving the discrete Boltzmann equation. During each timestep, two steps run - the streaming and the collision of the velocity distributions. The streaming is defined as:

$$f_k(t+1, \mathbf{x}) = f_k^{\text{post}}(t, \mathbf{x} + \mathbf{e}_{k'}) \quad (1)$$

where f_k is the k -th distribution function with its streaming vector \mathbf{e}_k , k' denotes the vector antiparallel to \mathbf{e}_k ($\mathbf{e}_k = -\mathbf{e}_{k'}$) and the superscript 'post' denotes the post-collision distribution function. According to this notation, $\mathbf{x} + \mathbf{e}_{k'}$ denotes the departure node of the k -th population being streamed to \mathbf{x} . Eq. (1) is written in a non-dimensionalized form with the timestep length and the lattice spacing equal to 1.

In this work, we use D2Q9 BGK model with 9 streaming directions ($k = 0, 1, \dots, 8$):

$$\mathbf{e}_k \in ((0, 0), (1, 0), (0, 1), (-1, 0), (0, -1), (1, 1), (-1, 1), (-1, -1), (1, -1)). \quad (2)$$

Due to the Lagrangian nature of the streaming step, such a choice of the streaming vectors imposes the use of a square lattice (refer to Fig. 1 for a graphical representation of the LBM lattice and streaming directions). The collision step calculates f_k^{post} from the current distributions and macroscopic fields. This work uses two relaxation time collision term [22]:

$$f_k^{\text{post}} = f_k(t, \mathbf{x}) - \frac{1}{\tau^+} [f_k^+(t, \mathbf{x}) - f_k^{\text{eq}+}(t, \mathbf{x})] - \frac{1}{\tau^-} [f_k^-(t, \mathbf{x}) - f_k^{\text{eq}-}(t, \mathbf{x})] \quad (3)$$

where τ^\pm , are relaxation times for the symmetric and anti-symmetric parts of the distributions, which are defined as:

$$\begin{aligned} f_k^+ &= \frac{f_k + f_{k'}}{2}, & f_k^- &= \frac{f_k - f_{k'}}{2} \\ f_k^{\text{eq}+} &= \frac{f_k^{\text{eq}} + f_{k'}^{\text{eq}}}{2}, & f_k^{\text{eq}-} &= \frac{f_k^{\text{eq}} - f_{k'}^{\text{eq}}}{2}. \end{aligned} \quad (4)$$

The relaxation times are related to each other by:

$$\Lambda = \left(\tau^+ - \frac{1}{2} \right) \left(\tau^- - \frac{1}{2} \right) \quad (5)$$

and we use the value of $\Lambda = 1/4$. The kinematic viscosity in the lattice units is then:

$$\nu_{lb} = c_s^2 \left(\tau^+ - \frac{1}{2} \right) \quad (6)$$

where $c_s = 1/\sqrt{3}$ denotes the lattice speed of sound. The equilibrium distributions f_k^{eq} are expressed as:

$$f_k^{\text{eq}}(t, \mathbf{x}) = \omega_k \rho_{lb} \left[1 + \frac{\mathbf{e}_k \cdot \mathbf{u}_{lb}}{c_s^2} + \frac{(\mathbf{e}_k \cdot \mathbf{u}_{lb})^2}{2c_s^4} - \frac{\mathbf{u}_{lb}^2}{2c_s^2} \right] \quad (7)$$

where ω_k is the weight specific to the k -th streaming direction:

$$\omega = \left(\frac{4}{9}, \frac{1}{9}, \frac{1}{9}, \frac{1}{9}, \frac{1}{9}, \frac{1}{36}, \frac{1}{36}, \frac{1}{36}, \frac{1}{36} \right). \quad (8)$$

The macroscopic density and velocity, $\rho_{lb} = \rho_{lb}(t, \mathbf{x})$ and $\mathbf{u}_{lb} = \mathbf{u}_{lb}(t, \mathbf{x})$ respectively, at time t and point \mathbf{x} , are obtained from the discrete populations:

$$\begin{aligned} \rho_{lb} &= \sum_{k=1}^q f_k \\ \mathbf{u}_{lb} &= \frac{1}{\rho_{lb}} \sum_{k=1}^q f_k \mathbf{e}_k \end{aligned} \quad (9)$$

The pressure is related to the density via the lattice speed of sound: $p_{lb} = \rho_{lb} c_s^2$.

In the numerical implementations, at each time step, Eq. (3) is first calculated to obtain the values of the post-collision distribution function (*collision step*). Then, (1) advects post-collision distributions to neighboring nodes (*streaming step*). Because lattice nodes \mathbf{x} coincide with the departure/arrival nodes of the streaming step, transport is purely Lagrangian and amounts to an index shift in the distribution function array.

The fixed relaxation time variants of LBM models assume $\tau^+ = 1$ [18, 19]. With $\Lambda = 1/4$, by Eq.(5) this sets $\tau^- = 1$ and with Eq.(4) simplifies the streaming and collision procedures from Eqs. (1) and (3) to the same form as if Bhatnagar-Gross-Krook collision [23] was used:

$$f_k(t+1, \mathbf{x}) = f_k^{\text{eq}}(t, \mathbf{x} + \mathbf{e}_{k'}). \quad (10)$$

This substitution alleviates the need to store the distribution function explicitly. In each timestep, the equilibrium distributions are calculated directly from the current macroscopic fields according to Eq. (7) and summed as in Eq. (9) to obtain the macroscopic fields in the next time step.

2.2 Formulation of meshless LBM

The meshless LBM algorithm considered in this work belongs to the family of off-grid LBM [24, 25, 26, 27, 20]. Those methods trade the Lagrangian approach to solving the streaming step for the semi-Lagrangian or Eulerian method, such that the space and velocity discretizations get decoupled, and nodes no longer need to be arranged in a regular grid. In the implementations taking the semi-Lagrangian approach to solve the streaming step, like the one discussed here, the discretization points (so-called Eulerian nodes) need not coincide with the departure points of the distribution function (so-called Lagrangian nodes). Instead, with each Eulerian point \mathbf{x}_i we identify q Lagrangian points to which the corresponding distributions are interpolated and from which they are advected during the streaming step (see Fig. 1). To relate the Eulerian and Lagrangian nodes' positions to one another, in MLBM the streaming vectors need to be expressed in physical units: $\delta \mathbf{x}_k = \mathbf{e}_k \delta x$ where δx is the streaming distance. In this manner, the positions of the departure nodes of the k -th population are related to the positions of their Eulerian nodes as $\mathbf{x} + \delta \mathbf{x}_{k'}$. We introduce the interpolation step between the collision and the streaming to approximate the distributions in the appropriate Lagrangian points. Once the approximation is done, the streaming and the collision step are performed in the same way as in LBM (see Fig. 2). We note that in the models with zero-velocity population discretized (i.e. \mathbf{e}_0 in Eq. (2)), one does not perform the streaming for this population explicitly.

Among many interpolation methods available to solve the streaming step on irregular discretizations, meshless methods [28, 29, 30] are less computationally demanding and error-prone in the discretization process, they achieve boundary-compliant discretizations, offer high order approximations as well as feasible local refinement and adaptivity. Such approaches have been frequently used to solve transport partial differential equations [31, 32, 33, 34, 35, 36].

The semi-Lagrangian streaming step in the discussed MLBM uses meshless interpolation in radial basis functions [28]. This allows one to approximate the value of a linear operator \mathcal{L} applied to the underlying function in an arbitrary point as a linear combination of the known function values stored in the neighboring nodes:

$$\mathcal{L}(f)|_{\mathbf{x}_0} \approx \sum_{i=1}^{N_L} f(\mathbf{x}_i) w_i \quad (11)$$

where \mathbf{x}_0 denotes the approximation point, \mathbf{x}_i denote the N_L approximation stencil members and w_i are interpolation weights. In particular one can speak of the unit operator \mathcal{L} ($\mathcal{L}(f) \equiv f$) which results in the interpolation formula in Eq. (11). To increase the algorithm's speed we use local approximation supports for each Lagrangian node consisting of its $N_L = 25$ closest neighbors, unless otherwise stated. To achieve high-order approximation we use polynomial augmentation [37] of order two, unless otherwise stated. For a detailed description of the algorithm, we refer the reader to our previous work [20].

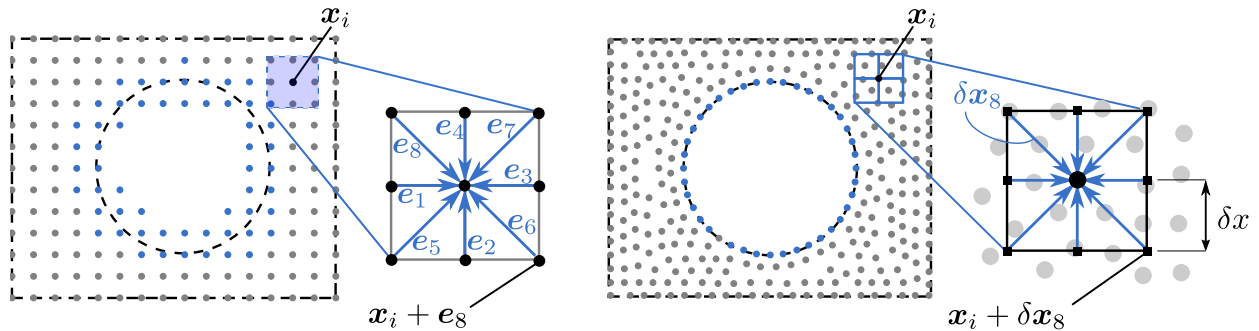


Figure 1: Comparison of space discretizations in the standard (*left*) and meshless (*right*) LBM. The standard LBM requires a square grid; the meshless LBM can operate on scattered, boundary-compliant node sets. Note that in MLBM, velocity is still discretized using a lattice, resulting in several departure points (so-called Lagrangian nodes, filled squares) assigned to each discretization point (so-called Eulerian nodes, filled circles).

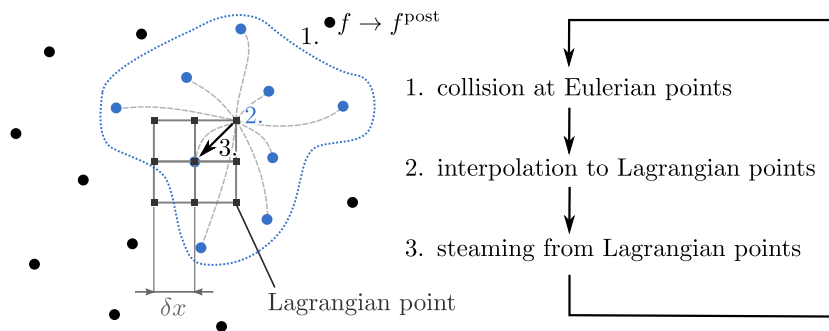


Figure 2: The procedure performed at a single timestep of the meshless LBM algorithm. Circles represent Eulerian points; squares denote Lagrangian points. A dashed loop encloses the stencil of a Lagrangian node, which consists of the nine closest neighbors of the Lagrangian node (blue circles). The interpolated distribution function is streamed to the Eulerian point at the center of the presented square lattice.

The application of the above formalism to LBM1 is the following. The macroscopic density and velocities are interpolated to each of the Lagrangian points. Then, the equilibrium distributions are calculated in the Lagrangian nodes, Eq.(7), and their values are summed according to Eq.(9) to obtain the next-timestep macroscopic fields in the Eulerian nodes. The interpolation of the macroscopic fields, and not the equilibrium distributions, frees one from the need to store f_k^{eq} in the memory.

2.3 Increasing Reynolds number in meshless LBM

To assess the ratio between inertial and viscous forces in a flow, the dimensionless Reynolds number is used:

$$Re = \frac{UL}{\nu} \quad (12)$$

arising naturally from non-dimensionalization of incompressible Navier-Stokes momentum equation:

$$\begin{aligned} \frac{\partial \mathbf{u}}{\partial t} + (\mathbf{u} \cdot \nabla) \mathbf{u} &= -\frac{\nabla p}{\rho} + \mathbf{g} + \nu \nabla^2 \mathbf{u} \\ \frac{\partial \mathbf{u}^*}{\partial t^*} + (\mathbf{u}^* \cdot \nabla^*) \mathbf{u}^* - \nabla^* p + \mathbf{g}^* &+ \frac{1}{Re} \nabla^{*2} \mathbf{u}^* \end{aligned} \quad (13)$$

$$\text{where } \mathbf{x}^* = \mathbf{x}/L, \quad \mathbf{u}^* = \mathbf{u}/U, \quad t^* = t \frac{U}{L} = tT, \quad p^* = p/\rho U^2, \quad \mathbf{g}^* = \mathbf{g} \frac{U^2}{L}$$

where asterisk denotes non-dimensionalized quantities, ν is the fluid's kinematic viscosity, \mathbf{g} is the acceleration, and L, U, T denotes the reference length, velocity, and time, respectively. Conventionally, when inertial forces dominate the system, the Reynolds number is larger than unity $Re > 1$. The practical utility of the Reynolds number lies in its ability to relate flows of different length and time scales to each other, e.g., flow past a real object versus its scaled model used in an experiment. The dependence of hydrodynamic coefficients, like drag, lift, or permeability, is often presented in relation to Re , thus making the results more universal. Reynolds

number also allows us to estimate the relative importance of non-linearity, turbulence, and momentum diffusion phenomena in a flow when choosing an appropriate physical model to describe the system.

In MLBM, the streaming distance length δx can be varied independently from the positions of the nodes discretizing the domain. It means that the whole space spanned by the streaming distance δx and the Eulerian discretization parameter h is available in MLBM, in contrast to traveling along the $\delta x = h$ line in the standard LBM (see Fig. 3). For instance, consider a flow domain of size $L = 100$. Let us assume that the streaming distance is $\delta x = 0.1$ (we do this by specifying the positions of Lagrangian points to differ from their Eulerian lattice centers by $\delta \mathbf{x}_k$ vectors). With such choice of L and δx we arrive at the domain size in lattice units equal to $L_{lb} = L/\delta x = 1000$, no matter what Eulerian discretization parameter h we choose. Now, increasing the size of the domain L , e.g., by multiplying the position vectors of the Eulerian points \mathbf{x}_i by some constant α_E (with δx unaltered) changes the domain size in lattice units α_E times. The same effect can be achieved by multiplying the streaming distance by $\alpha_\delta = 1/\alpha_E$ and keeping the positions of Eulerian points constant (we use the notation α_δ to distinguish the factor for the scaling of the streaming distance from the one for the scaling of the Eulerian points positions). This is because the approximation coefficients w_i from Eq. (11) are invariant under translation, rotation, and scaling of the stencil nodes and the interpolation point, and the presented MLBM algorithm uses the non-dimensionalized formulation of LBM ($\delta x = 1$ and $\delta t = 1$ in lattice units).

Both strategies (depending on scaling the domain size in physical units or the streaming distance length) alter the flow's Reynolds number in the following ways. Considering the Reynolds number calculated from the quantities in lattice units, both strategies change the size of the domain, changing the L_{lb} value from the previous paragraph. The same happens with Re calculated using the quantities in physical units when the α_E scaling is used. Finally, when the scaling is applied to the streaming distance (i.e. $\delta x \rightarrow \alpha_\delta \delta x$), to keep the physical viscosity unchanged, timestep length must scale with the square of α_δ , since $\nu = c_s^2(\tau - 1/2)\delta x^2/\delta t$. When this happens, the physical velocity U changes into its counterpart in the scaled setup U^δ as

$$U = U_{lb} \frac{\delta x}{\delta t} \rightarrow U^\delta = U_{lb} \frac{\delta x \alpha_\delta}{\delta t \alpha_\delta^2} = U \frac{1}{\alpha_\delta} \quad (14)$$

which in the case of decreasing the streaming distance ($\alpha_\delta < 1$) means increasing the velocity U in physical units.

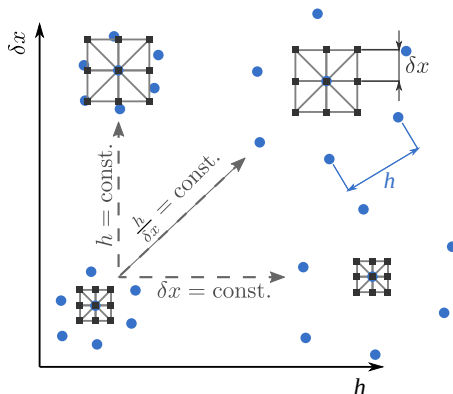


Figure 3: The $\delta x - h$ discretization parameters space and its three discussed directions (denoted by gray dashed arrows). Blue circles denote Eulerian points, and small dark gray squares denote Lagrangian nodes. Moving along each of the shown directions results in different scaling of the streaming length δx and Eulerian discretization parameter h . In particular, in LBM, moving only along the constant $\delta x/h$ direction is possible.

In general, the scaling of the streaming distance is followed by the scaling of the conversion factors from lattice units to physical units:

$$\begin{aligned} C_L = \delta x &\rightarrow C_L^\delta = \delta x \alpha_\delta = C_L \alpha_\delta \\ C_t = \delta t &\rightarrow C_t^\delta = \delta t \alpha_\delta^2 = C_t \alpha_\delta^2 \\ C_u = \delta x / \delta t &\rightarrow C_u^\delta = \delta x \alpha_\delta / \delta t \alpha_\delta^2 = C_u / \alpha_\delta \\ C_\nu = \delta x^2 / \delta t &\rightarrow C_\nu^\delta = C_\nu \\ C_g = \delta x / \delta t^2 &\rightarrow C_g^\delta = \delta x \alpha_\delta / \delta t^2 \alpha_\delta^4 = C_g / \alpha_\delta^3 \end{aligned} \quad (15)$$

Having noticed the equivalence of the scaling by the factor α_E or $\alpha_\delta = 1/\alpha_E$, in the remainder of this text, we will consider only the scaling of the Eulerian nodes positions (by α_E). We also note that the discussed method of increasing the Reynolds number in MLBM should apply when Eulerian schemes are used for solving

the streaming step[38]. The scaled streaming distance would then be equivalent to the scaled streaming velocity in the term $\mathbf{c} \cdot \nabla$ of the Boltzmann equation, where \mathbf{c} is the microscopic population velocity.

3 Results

We first present the results for an arbitrary value of the relaxation time. Consider a two-dimensional flow over a circular obstacle (see Fig. 4). The boundary conditions are no-slip walls on the obstacle's surface and far-field boundary with velocity in LBM units $U_{0,lb} = 0.04$ and uniform density $\rho_0 = 1$. The no-slip boundary is implemented via a multireflection bounce-back rule presented by Ginzburg and d'Humières [39]. Far-field boundary populations are taken to be equilibrium populations parametrized with the prescribed velocity and density. The initial condition are the equilibrium distributions parametrized with density $\rho_{lb} = 1$ and potential flow velocities [40] with a perturbation in the angular component introduced to force vortex shedding:

$$\begin{aligned} u_r &= U_0 \cos \theta \left(1 - \frac{4\mathbf{x}^2}{d^2} \right) \\ u_\theta &= -U_0 (-0.1 + \sin \theta) \left(1 + \frac{4\mathbf{x}^2}{d^2} \right), \quad \theta = \text{atan}(x, y) \end{aligned} \quad (16)$$

We use a discretization of the problem with Eulerian nodes corresponding to the domain height 2.5 and length

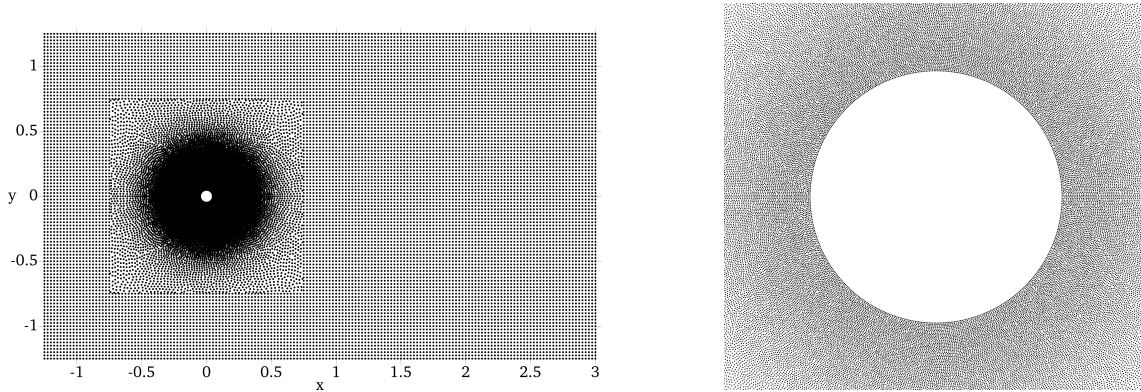


Figure 4: The hybrid regular-irregular discretization of the flow over a cylindrical obstacle used in the simulations (*left*) and a zoom in at the discretization around the obstacle (*right*).

4.25, the obstacle diameter $d = 0.1$, and its center located within a distance of 1.25 from the left boundary. The distance between the Eulerian nodes varies from $1/40$ away from the obstacle to $1/1600$ on the obstacle's surface. We use an irregular discretization in a square of side length 1.5 centered in the origin and a regular discretization elsewhere. This is motivated by the fact that for nodes away from the obstacle, the ratio $\delta x/h$ is too small to grant appropriate accuracy of interpolation with irregular points arrangement, which resulted in spurious oscillations near the left boundary corners [41, 42]. The set of Eulerian points is symmetric with respect to the $y = 0$ line. We perform five simulations on the same set of Eulerian nodes and with the same value of $U_{0,lb}$ but scaling the Eulerian points position vectors by factors of $\alpha_E = 1, 1.25, 1.5, 1.75, 2$. In this way, we increase the reference length of the problem L from Eq. (12). The LBM discretization parameters are: the streaming distance $\delta x = 6.25 \cdot 10^{-4}$, timestep length $\delta t = 3.125 \cdot 10^{-8}$ and relaxation time $\tau = 0.74$. The Reynolds number of each case was calculated based on the inlet velocity U_0 and the cylinder's diameter:

$$Re = \frac{U_0 \alpha_E d}{\nu} \quad (17)$$

We investigate the onset of inertial effects in the flow qualitatively by observing the appearance of the Kármán vortex street in the obstacle's wake and quantitatively via the increase of the Strouhal number and changes in time profiles of the cylinder's drag and lift coefficients.

Fig. 5 shows velocity streamlines of the channel flow for two extreme scaling factors α_E ($Re = 80, 160$). The onset of inertial effects is visible as the distance decreases between the repeating velocity field patterns in the obstacle's wake. Fig. 6 shows the values of the Strouhal number St against the Reynolds number of the flows. The Strouhal number is defined as:

$$St = \frac{f \alpha_E d}{U_0}, \quad (18)$$

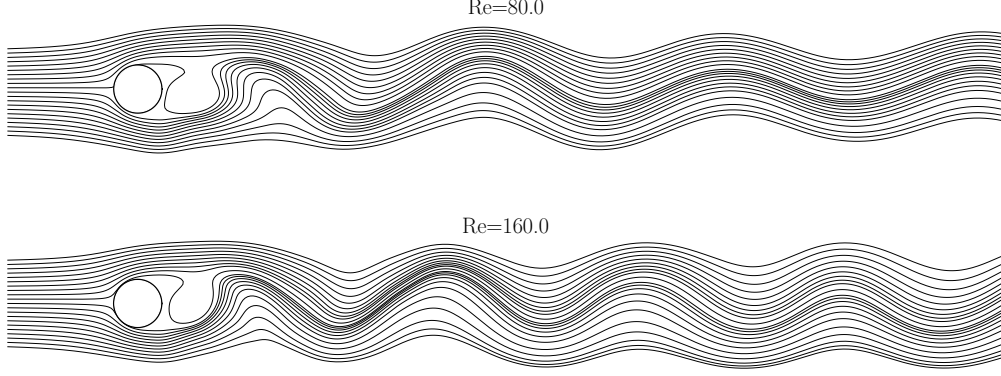


Figure 5: Streamlines of the velocity fields of the flow over a cylindrical obstacle for Reynolds numbers 80 and 160. The Reynolds number increase was achieved by rescaling the Eulerian points position vectors by the factors of 1 and 2, respectively. For clarity of view, the plot with $\alpha_E > 1$ was rescaled by $1/\alpha_E$ prior to plotting, and only a part of the whole domain is shown.

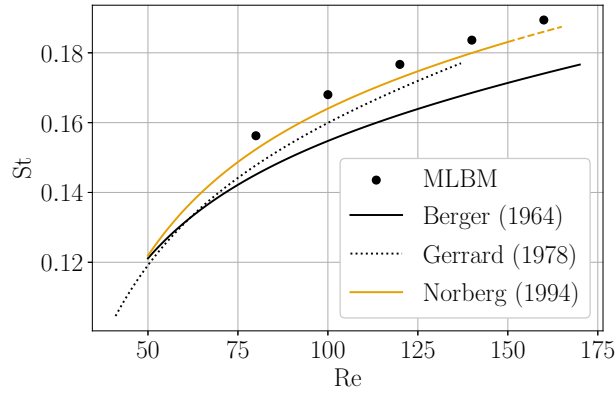


Figure 6: Strouhal number values achieved in flows around a cylindrical obstacle as a function of the flow's Reynolds number. The dashed part of the reference line for Norberg et al. [43] indicates the region where irregular shedding took place.

where f is the frequency of wake vortices shedding. The present results are in good agreement with a fit to the experimental data for the cylinder's diameter-to-length ratio equal to 2000 [43] and significantly higher compared to earlier experimental works [44, 45, 46].

Fig. 8 show the amplitudes of the lift coefficient C_L and the amplitudes and the mean values of the drag coefficient C_D compared with results from several works on off-grid LBM (OLBM)[47, 48] and experimental data adopted from [49]. The coefficients are defined as:

$$C_L = \frac{2F_L}{\rho U_0^2 d}, \quad C_D = \frac{2F_D}{\rho U_0^2 d}, \quad (19)$$

where F_L , F_D are lift and drag force, respectively. To calculate the tangent component of the hydrodynamic stress on the obstacle's surface we use the viscous stress tensor σ'_{ij} :

$$\sigma'_{ij} = \mu \left(\frac{\partial u_i}{\partial x_j} + \frac{\partial u_j}{\partial x_i} \right) \quad (20)$$

where μ is the dynamic viscosity of the fluid at constant density $\rho = 1$ and by u_i we mean the velocity components (i.e. $u_0 \equiv u$ and $u_1 \equiv v$). We approximate the derivatives using the same meshless basis as for the interpolation. The normal component of the stress is obtained from the pressure $p = p_{lb} \rho_{ref} \delta x^2 / \delta t^2$ where ρ_{ref} is the reference density. Each of N_B Eulerian nodes on the boundary is assigned a constant length element $\Delta L_B = \pi d \alpha_E / N_B$, and the stresses are integrated with piecewise constant integration. The exemplary time profiles of C_D and C_L for $Re = 160$ are shown in Fig. 7. The mean value of the lift coefficient (not shown in Fig. 8) is several orders of magnitude lower than its amplitude, which is a correct result (ideally, the mean

should be zero). The mean value of the drag coefficient decreases with Re , which is an expected result, being higher than the values reported by other works on OLBM. The amplitude of the lift/drag coefficient increases with Re , being slightly higher than the reference values.

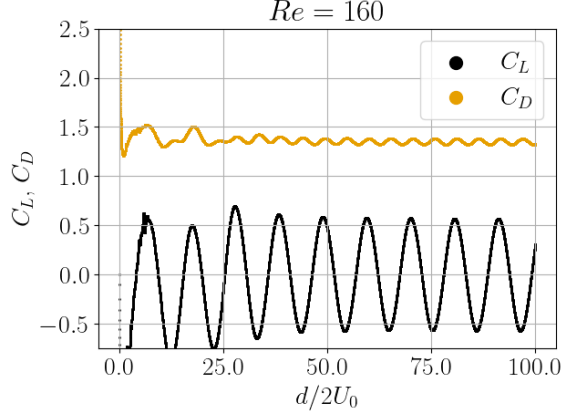


Figure 7: Time evolution of the drag (C_D) and lift (C_L) coefficients for $Re = 160$ case. Time is in units of $d/2U_0$.

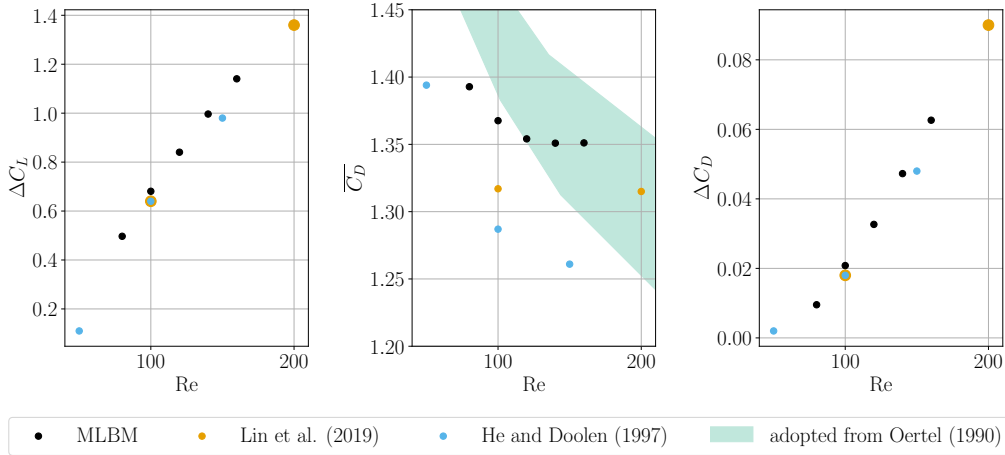


Figure 8: Aerodynamic coefficients for the flow over a cylindrical obstacle versus the Reynolds number. *Left*: the amplitudes of the lift coefficient. *Middle*: the means of the drag coefficient. *Right*: the amplitudes of the drag coefficient. Black symbols are present data; colored symbols are the data of He and Doolen [47] and Lin et al. [48]. The green area in the middle plot is the data of the mean C_D from various experimental works adopted from [49].

3.1 Application of MLBM1 in the lid-driven cavity

The flow domain is a $[0, 1] \times [0, 1]$ square (Fig. 9). We use irregular discretizations with the Eulerian discretization parameter $h = 1/160$ uniform in space. We set the top lid velocity to $u_{lb}(x, 1) = U_{0,lb}(1 - (2x^* - 1)^{24})$ where $U_{0,lb} = 0.1$ is the reference velocity in LB units and $x^* = \min(\max(0, x), 1)$ is the truncated x -coordinate. The no-slip boundary condition on the left, right, and bottom walls is implemented via multireflection bounce-back [39]. The unknown populations at the top boundary are equilibrium distributions parametrized with $\rho_{lb} = 1$ and velocities: $u_{lb}(x, 1)$ and $v_{lb}(x, 1) = 0$. We introduce x^* to be able to calculate f_k^{eq} streamed from $x < 0$ or $x > 1$. To increase the Reynolds number, we scale the positions of Eulerian points by the factor of $\alpha_E = 1, 4, 10, 32, 50$. Along with the streaming distance $\delta x = 6 \cdot 10^{-3}$ and physical viscosity $\nu = 1$, this gives Reynolds numbers based on the square side length and top lid velocity equal to 100, 400, 1000, 3200 and 5000. We initialize the simulation with equilibrium distributions parametrized with zero velocity and unit density and iterate the simulation until the relative change of the x -component of the velocity between two timesteps

defined as:

$$\Delta u = \frac{\max_i (|u_i^{n+1} - u_i^n|)}{U_0} \quad (21)$$

falls below 10^{-12} or up to $6 \cdot 10^6$ (for $\alpha_E = 32$) or $12 \cdot 10^6$ (for $\alpha_E = 50$) iterations. By u_i^n we mean the value of the x -component of the velocity at the i -th Eulerian node at the n -th timestep.

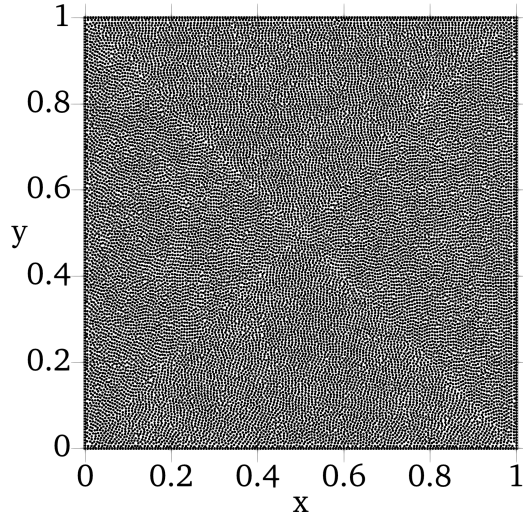


Figure 9: The irregular discretization used in the simulations of the flow in a driven cavity.

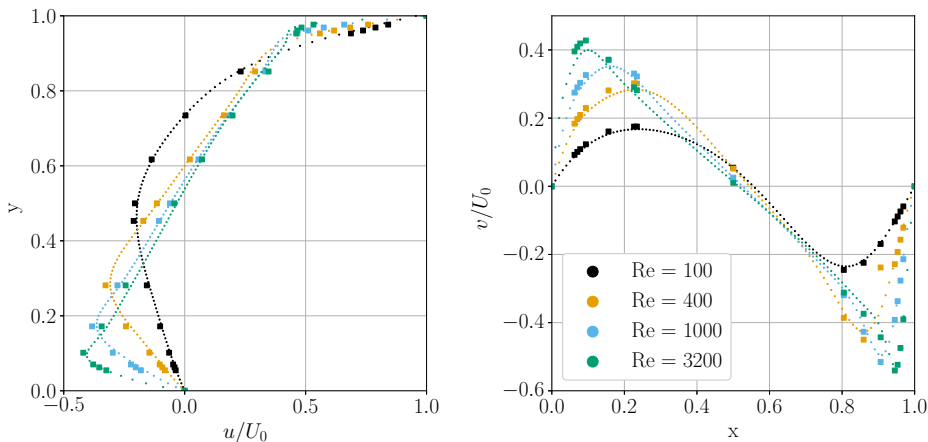


Figure 10: Profiles of u and v components of velocity along the lines $x = 0.5$ and $y = 0.5$ for the driven cavity flow. Small symbols denote MLBM1 results, larger squares denote the reference solution by Ghia [50]. Colors indicate the Reynolds number.

Figure 10 shows the normalized u and v component of velocity profiles along the centerlines of the cavity ($x = 0.5$, $y = 0.5$ after rescaling the domain by $1/\alpha_E$). Small circles denote MLBM1 results and are compared with the results of Ghia [50] denoted by larger squares. A good compliance between the two methods is visible, especially in the middle of the primary vortex. The difference in the velocity profiles increases closer to the boundaries, possibly due to large velocity gradients and shear stresses. Fig. 11 shows the centers of the primary vortex and the secondary vortices in the bottom left and bottom right corners of the cavity. The compliance between MLBM1 results and Ghia's solution [50] is within about 1% of the domain side length. As the $Re = 5000$ case exhibited an oscillatory behavior of slowly decreasing amplitude, we plot the path of the primary vortex and the secondary vortex in the bottom left corner of the cavity in Fig. 12. After $12 \cdot 10^6$ iterations, corresponding to $t = 72$, the centers of the vortices oscillate around points close to those reported by Ghia [50]. We note that to obtain a stable solution in $Re = 5000$ case, we needed to increase the order of augmentation in the meshless approximation to the fourth and the number of stencil members to $N_L = 70$.

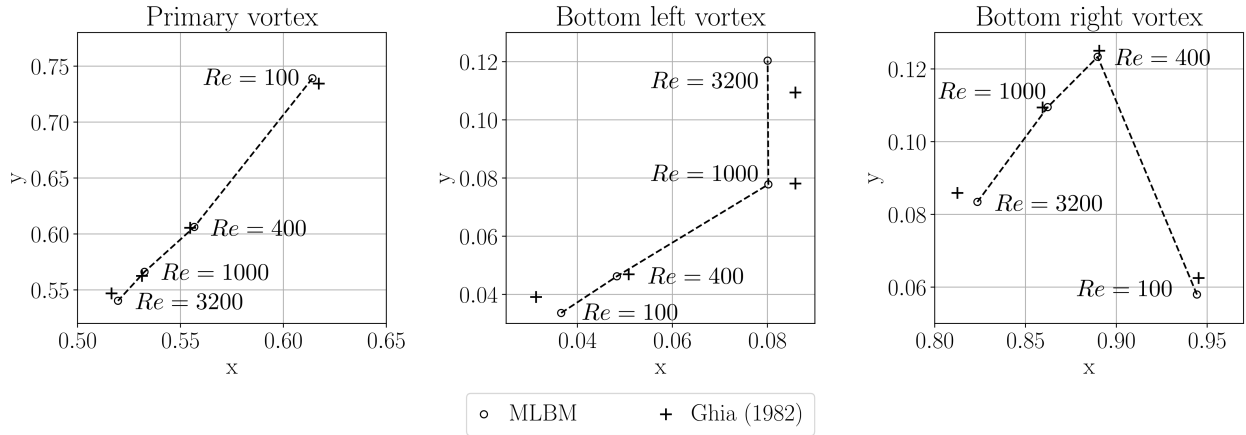


Figure 11: Positions of the centers of the vortices in the driven cavity. *Left*: the primary vortex, *center*: the secondary bottom left vortex and *right*: the secondary bottom right vortex. The dotted line denotes the sequence of increasing Re : 100, 400, 1000, 3200. The MLBM1 data are compared with the results of Ghia [50].

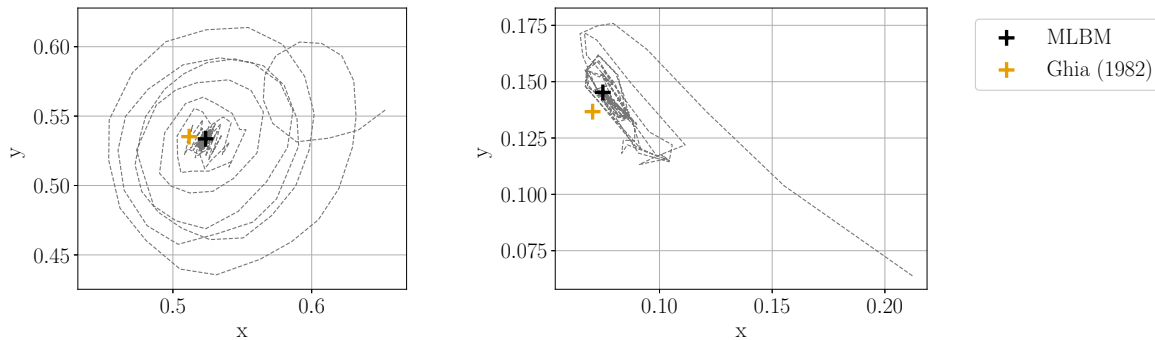


Figure 12: Paths traversed by the centers of the primary vortex (*left*) and the secondary bottom left vortex (*right*), $Re = 5000$. The MLBM1 data are compared with the vortices centers reported by Ghia [50].

Despite the stability, spurious shockwaves propagating from the right boundary could be seen throughout the simulation.

3.2 Inertial effects in a flow through a porous sample

We investigate the onset of inertial effects in a flow through a porous medium (see Fig. 13) of porosity $\phi = 0.64$ with MLBM1. We use irregular discretization with the Eulerian discretization parameter $h = 5 \cdot 10^{-3}$. The no-slip boundary condition is imposed on the top and bottom boundary and the circular obstacles' surfaces using the multireflection bounce back rule [39]. The periodic boundary condition is imposed on the left and right boundary by periodic search of the stencil members. The flow is forced by a constant acceleration of value $g_{lb} = 10^{-7}$ along the x direction. The meshless discretization of the domain corresponds to its size of 1×1 . The investigated values of the scaling parameter α_E range from 1 to 17. We note that for $\alpha_E = 18$, we could not obtain a stable solution despite increasing the stencil size to $N_L = 70$ and using fourth-order polynomial augmentation. The streaming distance length is chosen to be $\delta x = 2.5 \cdot 10^{-3}$, timestep length is $\delta t = 1.04 \cdot 10^{-6}$ and the kinematic viscosity is $\nu = 1$. The Reynolds number for each case was calculated based on the mean flow velocity in the x -direction $\langle u \rangle$:

$$\langle u \rangle = \frac{1}{\phi} \int_D d\Omega u(\mathbf{x}), \quad (22)$$

sample's side length equal to α_E and kinematic viscosity ν .

We show the visualization of the velocity field for three chosen values of α_E in Fig. 14. As the Reynolds number increases, recirculation zones grow causing the streamlines to separate from the grains' wakes.

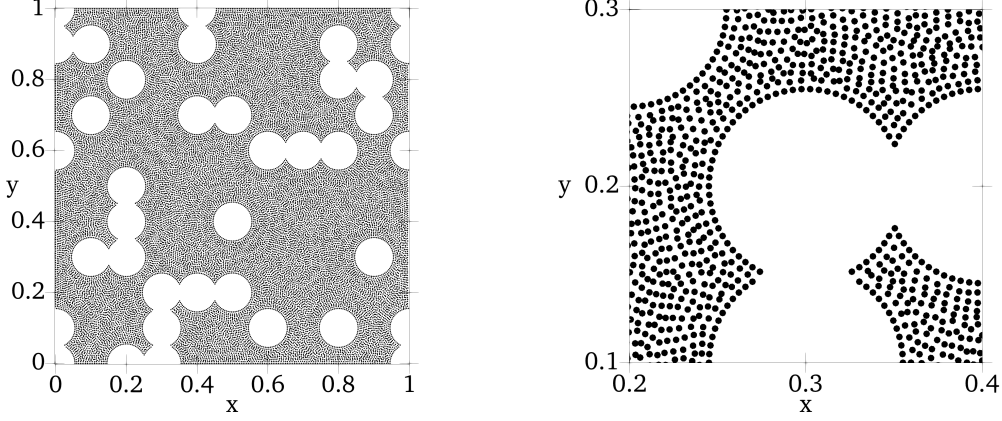


Figure 13: The point cloud used for the simulations of a flow through a porous sample: the whole discretized domain and a zoom at the discretization detail (*right*).

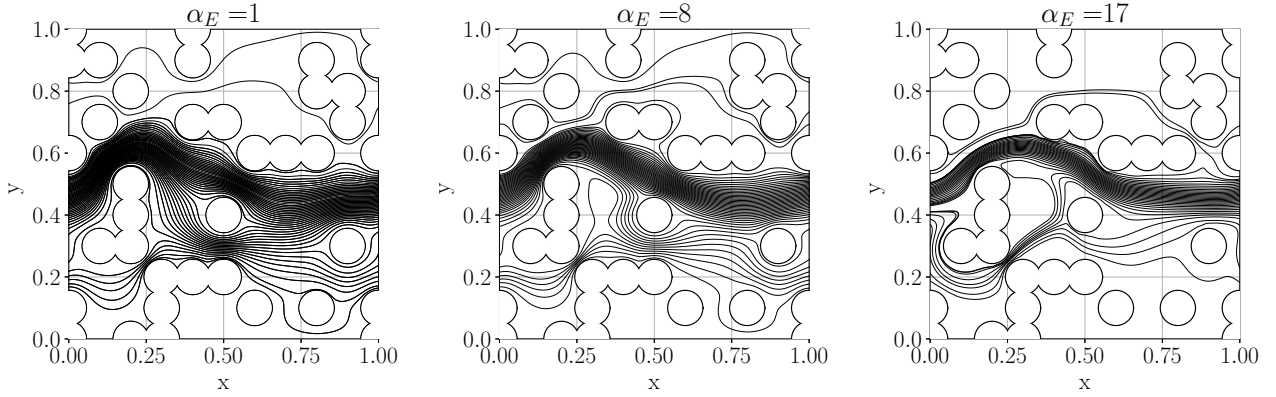


Figure 14: Streamlines of the velocity field of flows through the porous domain scaled with the factors $\alpha_E = 1, 8, 17$ ($Re = 0.76, 305, \text{ and } 1511$, respectively). The points coordinates were rescaled by a factor of $1/\alpha_E$ prior to plotting.

The inertial effects appearance can be quantified in terms of kinetic energy distribution in the system [5]. The left plot in Fig. 15 shows the fraction of the kinetic energy defined as $e_k(\mathbf{x}) = \mathbf{u}^2(\mathbf{x})$ confined in vortices to the total kinetic energy in the system:

$$\frac{\int_{\mathbf{x}: Q < 0} e_k(\mathbf{x}) d\Omega}{\int e_k(\mathbf{x}) d\Omega}. \quad (23)$$

We use the Q-criterion to define a vortex as a volume where:

$$Q = \frac{1}{2} (|S|^2 - |\Omega|^2) < 0, \text{ where } S = \frac{1}{2} \left(\frac{\partial u_i}{\partial x_j} + \frac{\partial u_j}{\partial x_i} \right), \Omega = \frac{1}{2} \left(\frac{\partial u_i}{\partial x_j} - \frac{\partial u_j}{\partial x_i} \right) \quad (24)$$

and $|A|^2 = \sum_{i,j} A_{ij}^2$. Similarly to Eq. (20), by u_i we mean the components of the velocity vector at a given point.

In the range of $Re = 100\text{--}700$ a rapid increase in the value of the fraction from Eq. (23) occurs.

We can relate this to the transition in the behavior of the $\langle u \rangle$. In the Darcy regime (inertial effects negligible), $\langle u \rangle$ is proportional to the pressure loss between the inlet and the outlet of the sample:

$$\langle u \rangle = -k \frac{\Delta P}{L\mu} = -k \frac{g}{\nu} \quad (25)$$

where k is the sample's permeability, L is the sample length, and the last equality holds if we relate the acceleration g forcing the flow to the mean pressure drop via $\rho g = \Delta P/L$. Next, Eq. (25) needs to be related to the changes in the size of the sample since this is the way of increasing Re in our study. If in Eq. (13) we omit the pressure gradient term and change the reference length from L to $\alpha_E L$, we find that the only difference

between the two systems (the one rescaled by α_E and the non-rescaled one) is in the term $Re = UL/\nu = L^2/T\nu$. This means that a system scaled by a factor of α_E behaves as if it was not scaled, but the viscosity was changed by a factor of α_E^{-2} (due to the term L^2 in the denominator of Re). Inserting this relation into Eq. (25) gives:

$$\langle u \rangle \propto k \frac{g}{\nu \alpha_E^{-2}} \propto \alpha_E^2 \quad (26)$$

A similar procedure applied in the Forchheimer regime (leaving only the second order term $\langle u \rangle^2$) yields:

$$\langle u \rangle^2 \propto \alpha_E^2. \quad (27)$$

Presenting Eqs. (26) and (27) in logarithmic scale gives:

$$\log \langle u \rangle \propto \begin{cases} 2 \log \alpha_E, & \text{Darcy regime} \\ \log \alpha_E, & \text{Forchheimer regime} \end{cases} \quad (28)$$

which is visible in the right plot of Fig. 15. The transition between the second and the first order relations, denoted by dashed grey lines in Fig. 15, occurs at the scaling factor $\alpha_E \approx 7$ for which $Re \approx 25$ (see the inset in the left subplot of Fig. 15) and corresponds well with the predictions of the onset of inertial effects from the vortices' kinetic energy approach.

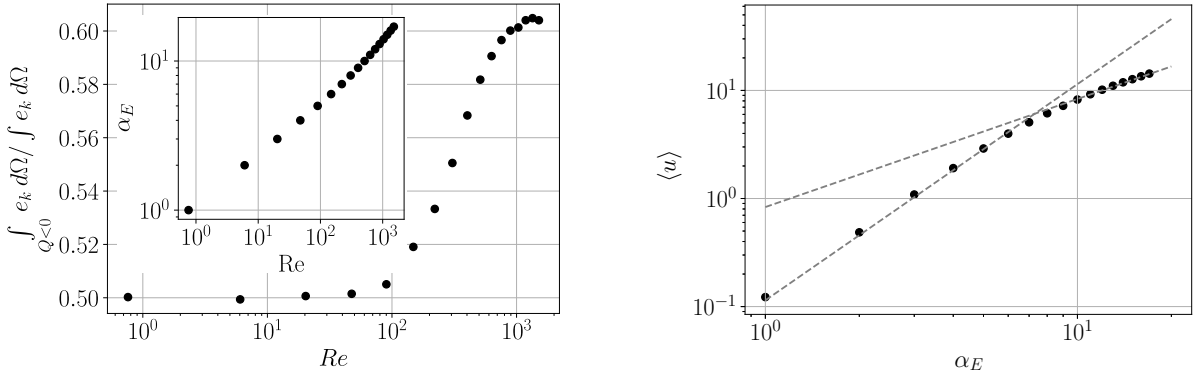


Figure 15: *Left*: the fraction of the kinetic energy confined in the $Q < 0$ volumes as a function of the Reynolds number. The inset shows the relation between the Reynolds number and the scaling factor α_E . *Right*: mean x -component velocity defined by Eq.(22) as a function of the scaling factor. The dashed lines denote the 1st and the 2nd order slopes.

Computational complexity and memory demands of the MLBM1 algorithm

Matyka and Dzikowski [18] derived the expression for the memory demands of their algorithm, which yields:

$$M_{\text{LBM1}} = N_{\text{LBM1}} \cdot 2N_f c \quad (29)$$

where N_{LBM1} is the number of nodes in the discretization, N_f is the number of macroscopic fields (in our case 3 - ρ, u and v), and c is the number of bytes per single number (e.g. 8 for `double`). MLBM1 uses additional memory to store the interpolation weight vectors for each of the $N(q-1)$ Lagrangian nodes (the term -1 appears because no interpolation is needed for the populations with zero microscopic velocity). Assuming that each interpolation stencil has the same number of nodes N_L , this results in the memory demands for MLBM1:

$$M_{\text{MLBM1}} = N_{\text{MLBM1}} \cdot (2N_f + N_L(q-1))c \quad (30)$$

where N_{MLBM1} is the number of Eulerian nodes. Taking the ratio of the two gives:

$$r_M = \frac{M_{\text{MLBM1}}}{M_{\text{LBM1}}} = \frac{N_{\text{MLBM1}}}{N_{\text{LBM1}}} \cdot \frac{2N_f + N_L(q-1)}{2N_f} = \frac{N_{\text{MLBM1}}}{N_{\text{LBM1}}} \cdot \left(1 + \frac{N_L(q-1)}{2N_f}\right) \quad (31)$$

In our case, $N_f = 3$, $q = 9$, and for most of the presented cases, $N_L = 25$. Considering that sparser discretizations can be used in the meshless algorithm, it turns out that MLBM1 can outperform LBM1 regarding memory demands for the same streaming distance value. For example, in the driven cavity flow, we used $\delta x = 6 \cdot 10^{-3}$, which would give the number of nodes in the LBM1 setup ranging from $2.8 \cdot 10^4$ for $\alpha_E = 1$ to $7 \cdot 10^7$ for

$\alpha_E = 50$. At the same time the term in brackets in Eq. (31) is equal to 34 for $\alpha_E < 50$ and 94 for $\alpha_E = 50$ (due to the change of N_L for $\alpha_E = 50$). This means that for the MLBM1 domain with $N = 22615$ Eulerian nodes, the ratio r_M ranges from 27 times more memory in the case of MLBM1 for $\alpha_E = 1$ to 32 more memory in the case of LBM1 for $\alpha_E = 50$. This shows the possibility of considerably reducing the number of nodes in LBM1 models with an off-grid (especially meshless) streaming procedure. When a proper local refinement strategy is used, this may come at an even lower cost to the solution's accuracy.

The computational complexity of MLBM1 carries the overhead of interpolation during the streaming step. To exploit the absence of explicit storage of the distribution function in the memory, the collision (i.e., the calculation of f_k^{eq}) must take place in Lagrangian nodes, and the macroscopic fields must be interpolated to those points. Otherwise (if the collision took place in Eulerian nodes), f_k^{eq} would have to be stored in memory between its calculation and interpolation. This means that for each Eulerian point, one needs $qO_{\text{col}} + (q-1)N_fO_{\text{int}}$ where O_{col} is the number of operations needed to calculate f_k^{eq} and O_{int} is the number of operations needed to interpolate a scalar within a stencil (note that for $k = 0$ one does not need to interpolate, but still the calculation of f_0^{eq} is necessary). This shows that the savings in memory for q distributions come at the cost of N_f times more interpolations which have to be done for each Lagrangian node, compared to MLBM (in MLBM, one interpolates only one population to each Lagrangian point). The nonlinearity of the discrete f_k^{eq} in velocities prohibits combining the collision and interpolation coefficients and simplifying the implementation of MLBM1.

4 Discussion

The decoupled space and velocity discretizations in MLBM change the paradigm of increasing the model's size typical for LBM and make it more similar to one of Navier-Stokes solvers. In LBM, the information about the characteristic size of the problem is encoded in the number of lattice links/nodes that discretize this size. So is the accuracy of the approximation in space. In MLBM, the information about the system's size is stored in the ratio between the streaming distance and the distance between Eulerian points representing the characteristic length. The approximation accuracy in space depends on the distances between the approximation stencil members. It is invariant under their translation, rotation, and scaling by a constant as long as the approximated function is devoid of discontinuities. Consequently, in MLBM, the velocity discretization parameters are determined by the desired compressibility errors. In contrast, the space discretization parameters are determined by the flow domain's geometry and the desired approximation accuracy in space. This is interpreted as hypervolumes in the space of those two groups of discretization parameters accessible to MLBM, where each point might be assigned its Reynolds number, in contrast to hypersurfaces in the case of LBM.

We chose the presented way of increasing the Reynolds number in MLBM to make the procedure as similar to the LBM approach as possible and highlight how the two methods relate to each other. This allows us to state the following. First, the qualitative results show that the described approach causes the Reynolds number to increase. It also suggests that the propagation of information in the model based on the approximation, rather than the exact streaming, does not impair the physical mechanism of mass and momentum transfer in the discrete Boltzmann equation. Large streaming distances compared to the spacings between the Eulerian points correspond to fast momentum diffusion, small $\delta x/h$ ratios - on the contrary. Second, quantitative analysis underlines the importance of the approximation accuracy for the solution. At the same time, the presented discretization parameters may serve as a crude estimation of the method's stability limits along with the aids to mitigate the divergence.

The accuracy and convergence of MLBM and other off-grid LBM methods were investigated in numerous works [26, 51, 20], especially in application to inertial flows in works by Lin and others [48] or Musavi and Ashrafizaadeh citeMusavi2019,Musavi2016. According to the findings by, e.g., Krämer and others [51], the decreasing ratio of $\delta x/h$ introduces more considerable approximation errors in OLB. When semi-Lagrangian streaming is used, this has directly to do with the error term $\mathcal{O}(h^{p+1}/\delta x)$ characteristic for semi-Lagrangian methods, as suggested in our previous work[20]. To prevent the divergence of this term, for the growing h , one would need to either increase δx , which would again decrease the size of the domain, or increase the accuracy of the approximation. We presented this procedure in two tests. First, we used regular space discretization in the far-field subdomain of the flow past a cylinder to avoid oscillations generated in the domain corners (in contrast to an irregular discretization around the cylinder). Second, in the driven cavity test for the highest Reynolds number ($Re = 5000$), the augmentation order and the number of stencil members were increased compared to the cases with lower Re to mitigate the divergence of the simulation. However, the mentioned flow through a porous medium for $\alpha_E = 18$ shows that increasing the approximation order or the stencil size does not always guarantee stability retrieval. In such cases, the Eulerian discretization refinement should be used. On the other hand, from the LBM error point of view, decreasing the $\delta x/h$ ratio acts in favor of the compressibility error, which would increase when higher Re would be achieved by larger inlet velocity or acceleration. Finally, the error of the solution obtained with MLBM on rescaled domains may also come from the under-resolution of

physical phenomena, such as small vortices typical for nearly turbulent flow. However, this under-resolution might be exploited to the method's advantage, as suggested by Chen [52].

The solution's accuracy considerations must always be counterbalanced by preserving the simulation's efficiency and robustness. In MLBM, one can look for memory and computational savings in discretizing space and velocity independently. First, the feasibility of the local static and dynamic discretization refinements in meshless approximation methods offers great promise to reduce the number of Eulerian points in MLBM compared to LBM. Apart from an arbitrary refinement, as shown in the present work in the case of the flow around a cylinder, the choice of a proper error indicator, such as quantities based on vorticity suggested by Fakhari and Lee [53] or on the velocity field divergence [15] can allow for dynamic h - or p -refinement during the simulation run to make the error of the solution more uniform in space granting a better accuracy at a little increase of the computational expense. Second, LBM1 models [18, 19] reduce the memory overhead by explicitly storing just a few macroscopic fields rather than a large number of velocity distributions. We show that by introducing meshless space discretization, it is possible to achieve a several-fold memory advantage in comparison to the lattice-based LBM1, which is already estimated to use about 76% less memory than its arbitrary relaxation time counterpart [18].

5 Conclusions

We investigate the new procedure to increase the Reynolds number of a flow from laminar to the transitional regime in meshless LBM simulations by increasing the system's domain size. We achieve this solely by multiplying the coordinates of Eulerian points by some constant $\alpha_E > 1$, or equivalently - the streaming distance by its inverse $1/\alpha_E$, thus no additional nodes are inserted into the domain. We apply this method of the Reynolds number increase to a general meshless LBM scheme and to the meshless implementation of a memory-efficient LBM model with the relaxation time $\tau = 1$ (LBM1). We show that the procedure works by numerically investigating three test cases in a range of Reynolds numbers - von Kármán vortex street behind a cylindrical obstacle of infinite length, driven cavity flow, and a flow through a porous sample. The qualitative observation of the velocity fields indicates the onset of inertial effects in the flows. Also, the obtained values of hydrodynamic parameters agree well with the numerical and experimental references in a wide range of Reynolds numbers. From the performed simulations, we estimate the possible memory savings of the meshless LBM1 compared to the standard (lattice-based) LBM1 to be as high as 32-fold and pinpoint the source of the computational overhead of the meshless LBM1.

Our findings open new perspectives for further studies on the development and applications of MLBM. Questions yet to be answered address the issues of the possibility of simultaneous scaling of space and velocity discretizations, or the detailed mechanism of the information propagation when the non-purely Lagrangian streaming step is used.

6 Acknowledgments

Funded by National Science Centre, Poland under the OPUS call in the Weave programme 2021/43/I/ST3/00228. This research was funded in whole or in part by National Science Centre (2021/43/I/ST3/00228). For the purpose of Open Access, the author has applied a CC-BY public copyright licence to any Author Accepted Manuscript (AAM) version arising from this submission.

References

- [1] D. N. Ku, Blood flow in arteries, *Annual review of fluid mechanics* 29 (1) (1997) 399–434.
- [2] D. H. Kelley, J. H. Thomas, Cerebrospinal fluid flow, *Annual Review of Fluid Mechanics* 55 (2023) 237–264.
- [3] M. R. Morad, A. Khalili, Transition layer thickness in a fluid-porous medium of multi-sized spherical beads, *Experiments in Fluids* 46 (2) (2009) 323–330.
- [4] M. Souzy, H. Lhuissier, Y. Méheust, T. Le Borgne, B. Metzger, Velocity distributions, dispersion and stretching in three-dimensional porous media, *Journal of Fluid Mechanics* 891 (2020) A16.
- [5] J. S. Andrade, U. M. S. Costa, M. P. Almeida, H. A. Makse, H. E. Stanley, Inertial effects on fluid flow through disordered porous media, *Phys. Rev. Lett.* 82 (1999) 5249–5252. doi:10.1103/PhysRevLett.82.5249.
URL <https://link.aps.org/doi/10.1103/PhysRevLett.82.5249>

- [6] R. Sánchez-González, S. W. North, Chapter 18 - nitric oxide laser-induced fluorescence imaging methods and their application to study high-speed flows, in: J. Laane (Ed.), *Frontiers and Advances in Molecular Spectroscopy*, Elsevier, 2018, pp. 599–630. doi:<https://doi.org/10.1016/B978-0-12-811220-5.00019-8>.
URL <https://www.sciencedirect.com/science/article/pii/B9780128112205000198>
- [7] C. Pan, L.-S. Luo, C. T. Miller, An evaluation of lattice boltzmann schemes for porous medium flow simulation, *Computers & fluids* 35 (8-9) (2006) 898–909.
- [8] C. Gao, R.-N. Xu, P.-X. Jiang, Pore-scale numerical investigations of fluid flow in porous media using lattice boltzmann method, *International Journal of Numerical Methods for Heat & Fluid Flow* 25 (8) (2015) 1957–1977.
- [9] M. Matyka, Z. Koza, How to Calculate Tortuosity Easily?, *AIP Conference Proceedings* 1453 (1) (2011) 17–22. doi:10.1063/1.4711147.
- [10] G. Falcucci, E. Jannelli, S. Ubertini, S. Succi, Direct numerical evidence of stress-induced cavitation, *Journal of Fluid Mechanics* 728 (2013) 362–375. doi:10.1017/jfm.2013.271.
URL https://www.cambridge.org/core/product/identifier/S0022112013002711/type/journal_article
- [11] R. C. Coelho, M. M. Doria, Lattice Boltzmann Method for Semiclassical Fluids, *Computers and Fluids* 165 (October 2017) (2018) 144–159. doi:10.1016/j.compfluid.2018.01.019.
- [12] A. J. Ladd, Numerical Simulations of Particulate Suspensions Via a Discretized Boltzmann Equation. Part 1. Theoretical Foundation, *Journal of Fluid Mechanics* 271 (1994) 285–309. doi:10.1017/S0022112094001771.
- [13] X. Sun, C. Zhang, X. Wang, A DNS investigation by LBM: Acoustic characteristics of a flow around rod-hydrofoil configuration at different angles of attack, *Ocean Engineering* 266 (2022) 112779. doi:10.1016/j.oceaneng.2022.112779.
URL <https://linkinghub.elsevier.com/retrieve/pii/S0029801822020625>
- [14] L. A. Hegele, A. Scagliarini, M. Sbragaglia, K. K. Mattila, P. C. Philippi, D. F. Puleri, J. Gounley, A. Randles, High-Reynolds-number turbulent cavity flow using the lattice Boltzmann method, *Physical Review E* 98 (4) (2018) 043302. doi:10.1103/PhysRevE.98.043302.
URL <https://link.aps.org/doi/10.1103/PhysRevE.98.043302>
- [15] S. Succi, *The Lattice Boltzmann Equation: For Complex States of Flowing Matter*, Oxford University Press, 2018. doi:10.1093/oso/9780199592357.001.0001.
- [16] T. Krüger, H. Kusumaatmaja, A. Kuzmin, O. Shardt, G. Silva, E. M. Viggen, *The Lattice Boltzmann Method: Principles and Practice*, Graduate Texts in Physics, Springer International Publishing, Cham, 2017. doi:10.1007/978-3-319-44649-3.
- [17] Z. Guo, C. Shu, *Lattice Boltzmann Method: And Its Applications in Engineering*, no. vol. 3 in *Advances in Computational Fluid Dynamics*, World Scientific, Singapore, 2013.
- [18] M. Matyka, M. Dzikowski, Memory-efficient lattice boltzmann method for low reynolds number flows, *Computer Physics Communications* 267 (2021) 108044. doi:<https://doi.org/10.1016/j.cpc.2021.108044>.
URL <https://www.sciencedirect.com/science/article/pii/S0010465521001569>
- [19] J. G. Zhou, Macroscopic Lattice Boltzmann Method, *Water* 13 (1) (2020) 61. doi:10.3390/w13010061.
URL <https://www.mdpi.com/2073-4441/13/1/61>
- [20] D. Strzelczyk, M. Matyka, Study of the convergence of the meshless lattice boltzmann method in Taylor–Green, annular channel and a porous medium flows, *Computers and Fluids* 269 (2024) 106122. doi:<https://doi.org/10.1016/j.compfluid.2023.106122>.
URL <https://www.sciencedirect.com/science/article/pii/S004579302300347X>
- [21] D. Strzelczyk, M. Rot, M. Matyka, G. Kosec, On meshless solution to Navier-Stokes problem in porous media: comparing meshless lattice Boltzmann method with ACM RBF-FD approach (in preparation) (2024).
- [22] I. Ginzburg, F. Verhaeghe, D. d’Humières, Two-Relaxation-Time Lattice Boltzmann Scheme: About Parametrization, Velocity, Pressure and Mixed Boundary Conditions, *Communications in Computational Physics*.

- [23] P. L. Bhatnagar, E. P. Gross, M. Krook, A Model for Collision Processes in Gases. I. Small Amplitude Processes in Charged and Neutral One-Component Systems, *Phys. Rev.* 94 (3) (1954) 511–525. doi:10.1103/PhysRev.94.511.
- [24] X. He, L. S. Luo, M. Dembo, Some Progress in Lattice Boltzmann Method. Part I. Nonuniform Mesh Grids, *Journal of Computational Physics* 129 (2) (1996) 357–363. doi:10.1006/jcph.1996.0255.
- [25] S. Ubertini, G. Bella, S. Succi, Lattice Boltzmann method on unstructured grids: Further developments, *Physical Review E* 68 (1) (2003) 016701. doi:10.1103/PhysRevE.68.016701. URL <https://link.aps.org/doi/10.1103/PhysRevE.68.016701>
- [26] A. Krämer, K. Küllmer, D. Reith, W. Joppich, H. Foysi, Semi-Lagrangian off-Lattice Boltzmann Method for Weakly Compressible Flows, *Physical Review E* 95 (2) (2017) 1–12. doi:10.1103/PhysRevE.95.023305.
- [27] S. H. Musavi, M. Ashrafizaadeh, A mesh-free lattice Boltzmann solver for flows in complex geometries, *International Journal of Heat and Fluid Flow* 59 (2016) 10–19. doi:10.1016/j.ijheatfluidflow.2016.01.006. URL <https://linkinghub.elsevier.com/retrieve/pii/S0142727X16300030>
- [28] M. Buhmann, Bengt Fornberg, Natasha Flyer: “A Primer on Radial Basis Functions with Applications to the Geosciences”, *Jahresbericht der Deutschen Mathematiker-Vereinigung* 119 (1) (2017) 53–58. doi:10.1365/s13291-016-0149-y.
- [29] W. Chen, Z. J. Fu, C. S. Chen, Recent Advances in Radial Basis Function Collocation Methods, no. 9783642395710, 2014. doi:10.1007/978-3-642-39572-7.
- [30] G. S. Bhatia, G. Arora, Radial Basis Function Methods for Solving Partial Differential Equations-A Review, *Indian Journal of Science and Technology* 9 (45). doi:10.17485/ijst/2016/v9i45/105079.
- [31] N. Flyer, G. B. Wright, Transport Schemes on a Sphere Using Radial Basis Functions, *Journal of Computational Physics* 226 (1) (2007) 1059–1084. doi:10.1016/j.jcp.2007.05.009.
- [32] V. Shankar, G. B. Wright, R. M. Kirby, A. L. Fogelson, Augmenting the Immersed Boundary Method with Radial Basis Functions (RBFs) for the Modeling of Platelets in Hemodynamic Flows, *International Journal for Numerical Methods in Fluids* 79 (10) (2015) 536–557. doi:10.1002/flid.4061.
- [33] V. Shankar, G. B. Wright, R. M. Kirby, A. L. Fogelson, A Radial Basis Function (RBF)-Finite Difference (FD) Method for Diffusion and Reaction-Diffusion Equations on Surfaces, *Journal of Scientific Computing* 63 (3) (2015) 745–768. doi:10.1007/s10915-014-9914-1.
- [34] G. Kosec, B. Šarler, Solution of Thermo-Fluid Problems by Collocation with Local Pressure Correction, *International Journal of Numerical Methods for Heat and Fluid Flow* 18 (7-8) (2008) 868–882. doi:10.1108/09615530810898999.
- [35] G. Kosec, A Local Numerical Solution of a Fluid-Flow Problem on an Irregular Domain, *Advances in Engineering Software* 120 (2016) 36–44. doi:10.1016/j.advengsoft.2016.05.010.
- [36] J. Slak, G. Kosec, Adaptive Radial Basis Function-Generated Finite Differences Method for Contact Problems, *International Journal for Numerical Methods in Engineering* 119 (7) (2019) 661–686. doi:10.1002/nme.6067.
- [37] N. Flyer, B. Fornberg, V. Bayona, G. A. Barnett, On the Role of Polynomials in RBF-FD Approximations: I. Interpolation and Accuracy, *Journal of Computational Physics* 321 (2016) 21–38. doi:10.1016/j.jcp.2016.05.026.
- [38] T. Lee, C. L. Lin, An Eulerian Description of the Streaming Process in the Lattice Boltzmann Equation, *Journal of Computational Physics* 185 (2) (2003) 445–471. doi:10.1016/S0021-9991(02)00065-7.
- [39] I. Ginzburg, D. d’Humières, Multireflection boundary conditions for lattice boltzmann models, *Phys. Rev. E* 68 (2003) 066614. doi:10.1103/PhysRevE.68.066614. URL <https://link.aps.org/doi/10.1103/PhysRevE.68.066614>
- [40] J. J. Bertin, *Aerodynamics for engineers* / John J. Bertin, 4th Edition, Prentice Hall, Upper Saddle River, NJ, 2002.
- [41] M. Jančić, M. Rot, G. Kosec, Spatially-varying meshless approximation method for enhanced computational efficiency (Apr. 2023). arXiv:2303.01760. URL <http://arxiv.org/abs/2303.01760>

- [42] G. Kosec, A local numerical solution of a fluid-flow problem on an irregular domain, *Advances in Engineering Software* 120 (2018) 36–44. doi:10.1016/j.advengsoft.2016.05.010.
URL <https://linkinghub.elsevier.com/retrieve/pii/S0965997816301065>
- [43] C. Norberg, An experimental investigation of the flow around a circular cylinder: Influence of aspect ratio, *Journal of Fluid Mechanics* 258 (1994) 287–316. doi:10.1017/S0022112094003332.
URL https://www.cambridge.org/core/product/identifier/S0022112094003332/type/journal_article
- [44] J. Gerrard, The wakes of cylindrical bluff bodies at low Reynolds number, *Philosophical Transactions of the Royal Society of London. Series A, Mathematical and Physical Sciences* 288 (1354) (1978) 351–382.
- [45] E. Berger, The determination of the hydrodynamic parameters of a karman vortex street from hot wire measurements at low reynolds number, *Z. Flugwiss* 12 (41) (1964) 41–59.
- [46] E. Berger, Transition of the laminar vortex flow to the turbulent state of the Karman vortex street behind an oscillating cylinder at low Reynolds number, *Jahrb. Wiss. Gess. LR* 164.
- [47] X. He, G. Doolen, Lattice Boltzmann Method on Curvilinear Coordinates System: Flow around a Circular Cylinder, *Journal of Computational Physics* 134 (2) (1997) 306–315. doi:10.1006/jcph.1997.5709.
- [48] X. Lin, J. Wu, T. Zhang, A Mesh-Free Radial Basis Function–Based Semi-Lagrangian Lattice Boltzmann Method for Incompressible Flows, *International Journal for Numerical Methods in Fluids* 91 (4) (2019) 198–211. doi:10.1002/flid.4749.
- [49] H. Oertel, Wakes Behind Blunt Bodies, *Annu. Rev. Fluid Mech.* 22 (1990) 539–64.
- [50] U. Ghia, K. N. Ghia, C. T. Shin, High-Re Solutions for Incompressible Flow Using the Navier-Stokes Equations and a Multigrid Method, *Journal of Computational Physics* 48 (3) (1982) 387–411. doi:10.1016/0021-9991(82)90058-4.
- [51] A. Krämer, D. Wilde, K. Küllmer, D. Reith, H. Foyssi, W. Joppich, Lattice Boltzmann simulations on irregular grids: Introduction of the NATriuM library, *Computers & Mathematics with Applications* 79 (1) (2020) 34–54. doi:10.1016/j.camwa.2018.10.041.
URL <https://linkinghub.elsevier.com/retrieve/pii/S0898122118306382>
- [52] H. Chen, Volumetric formulation of the lattice Boltzmann method for fluid dynamics: Basic concept, *Physical Review E* 58 (3) (1998) 3955–3963. doi:10.1103/PhysRevE.58.3955.
URL <https://link.aps.org/doi/10.1103/PhysRevE.58.3955>
- [53] A. Fakhari, T. Lee, Finite-difference lattice Boltzmann method with a block-structured adaptive-mesh-refinement technique, *Physical Review E* 89 (3) (2014) 033310. doi:10.1103/PhysRevE.89.033310.
URL <https://link.aps.org/doi/10.1103/PhysRevE.89.033310>